

Galaxy-galaxy strong lens perturbations: line-of-sight haloes versus lens subhaloes

Qiuhan He¹*, Ran Li^{2,3}†, Carlos S. Frenk¹, James Nightingale^{1,4}, Shaun Cole¹, Nicola C. Amorisco¹, Richard Massey^{1,4}, Andrew Robertson⁵, Amy Etherington^{1,4}, Aristeidis Amvrosiadis¹, Xiaoyue Cao^{2,3}

¹*Institute for Computational Cosmology, Department of Physics, Durham University, South Road, Durham DH1 3LE, UK*

²*National Astronomical Observatories, Chinese Academy of Sciences, 20A Datun Road, Chaoyang District, Beijing 100012, China*

³*School of Astronomy and Space Science, University of Chinese Academy of Sciences, Beijing 100049, China*

⁴*Centre for Extragalactic Astronomy, Department of Physics, Durham University, South Rd, Durham, DH1 3LE, UK*

⁵*Jet Propulsion Laboratory, California Institute of Technology, 4800 Oak Grove Drive, Pasadena, CA 91109, USA*

Accepted XXX. Received YYY; in original form ZZZ

ABSTRACT

We rederive the number density of intervening line-of-sight haloes relative to lens subhaloes in galaxy-galaxy strong lensing observations, where these perturbers can generate detectable image fluctuations. Previous studies have calculated the detection limit of a line-of-sight small-mass dark halo by comparing the lensing deflection angles it would cause, to those caused by a subhalo within the lens. However, this overly simplifies the difference in observational consequences between a subhalo and a line-of-sight halo. Furthermore, it does not take into account degeneracies between an extra subhalo and the uncertain properties of the main lens. More in keeping with analyses of real-world observations, we regard a line-of-sight halo as detectable only if adding it to a smooth model generates a statistically significant improvement in the reconstructed image. We find that the number density of detectable line-of-sight perturbers has been overestimated by as much as a factor of two in the previous literature. For typical lensing geometries and configurations, very deep imaging is sensitive to twice as many line-of-sight perturbers as subhaloes, but moderate depth imaging is sensitive to only slightly more line-of-sight perturbers than subhaloes.

Key words: dark matter – gravitational lensing: strong

1 INTRODUCTION

The most fundamental prediction of the cold dark matter (CDM) cosmological model is the existence of a large population of low mass dark matter haloes (Green et al. 2005; Diemand et al. 2007; Springel et al. 2008; Frenk & White 2012; Wang et al. 2020). This feature can be used to test the CDM model rigorously or to distinguish it from models with alternative types of dark matter. For example, the warm dark matter (WDM) model predicts a cutoff in the power spectrum of initial density perturbations, induced by particle free streaming, which translates into a cutoff in the halo mass function at a mass scale that depends on the WDM particle mass (Colín et al. 2000; Lovell et al. 2012; Schneider et al. 2012; Bose et al. 2016).

Recent observations have revealed a line in the X-ray spectra of galaxies and galaxy clusters at 3.5 keV that could result from

decay of a WDM particle such as a 7 keV sterile neutrino (Boyarsky et al. 2014; Bulbul et al. 2014, but see Riemer-Sørensen 2016). In this case, the halo mass function today would exhibit a sharp cutoff at a mass, $m_{200} \lesssim 10^8 M_\odot$. Thus, this model would be conclusively ruled out if one could demonstrate the existence of a population of haloes below this mass scale. Conversely, the CDM model would be conclusively ruled out if such a population were not found. Haloes that are of mass $m_{200} \lesssim 3 \times 10^8 M_\odot$ today were never able to make stars and therefore remain completely dark (see Benítez-Llambay & Frenk 2020; Sawala et al. 2016, and references therein). Such haloes cannot therefore be detected by conventional means but they can, in principle, be detected through their gravitational lensing effects.

Strong lensing systems that exhibit giant arcs or Einstein rings can appear measurably perturbed if any of the light from the source passes sufficiently close to a small dark halo (Koopmans 2005; Vegetti & Koopmans 2009a,b; Vegetti et al. 2012; Hezaveh et al. 2016; Li et al. 2016). This is a difficult measurement but applying sophisticated data analysis and modelling tools to high resolution imagery, it is possible to detect small haloes projected near the

* E-mail: qiuhan.he@durham.ac.uk

† E-mail: ranli@bao.ac.cn

2 *Q. He et al.*

Einstein radius of the lens and infer their mass (e.g. Koopmans 2005; Vegetti & Koopmans 2009a). The mass detection limit for dark matter haloes depends on the resolution of the image. With Hubble Space Telescope (HST) imagery, Vegetti et al. (2010) discovered a dark perturber of mass, $3.51 \pm 0.15 \times 10^9 M_\odot$, which they interpret as a subhalo in the strong lens system SDSS J0946+1006 (the mass here refers to that of a truncated pseudo-Jaffe density profile). Another dark object of mass, $1.9 \pm 0.1 \times 10^8 M_\odot$, was found in a lens galaxy at redshift $z = 0.88$ from even higher resolution imaging using adaptive optics at the Keck telescope (Vegetti et al. 2012).

To constrain the nature of the dark matter with this technique it is, of course, necessary to know the expected number of lensing perturbers in CDM and other models of interest. The perturbers can be either subhaloes of the main lens or “field” haloes that are not part of the main lens but appear projected near its Einstein radius. In what follows, we will refer to the latter as “line-of-sight” or “intervening” haloes or perturbers.

To count the expected number of subhaloes and intervening haloes consistently, Li et al. (2017, hereafter Li17) derived an effective mass, $M_{\text{eff}}(M_{\text{los}})$, for a line-of-sight halo of mass, M_{los} . This is determined by fitting a lensing image perturbed by an NFW halo at the lens redshift to the image perturbed by a line-of-sight halo of mass, M_{los} , at redshift, z_{los} . In other words, if a subhalo of mass, $M_{\text{eff}}(M_{\text{los}})$, can be detected, a line-of-sight halo of mass, M_{los} , should also be detected. In this way, one can calculate the effective mass function of all perturbers. Li17 showed that, for CDM, the number of detectable line-of-sight perturbers is 3-4 times larger than the number of subhalo perturbers.

A similar analysis was performed by (Despali et al. 2018, hereafter D18), who derived a fitting formula for M_{eff} by fitting the deflection angle of a lensing system containing a line-of-sight perturber to that of a system containing a subhalo. The analysis was performed for lenses with different image and redshift configurations. In agreement with the results of Li17, they found that the contribution from CDM line-of-sight haloes is about 3 times that from subhaloes for lenses with $z_l = 0.2$ and $z_s = 1.0$, and about 10 times that from subhaloes for lenses with $z_l = 0.5$ and $z_s = 2.0$. Besides, by statistically studying low mass haloes’ perturbation, Çağan Sengül et al. (2020) also show that line-of-sight perturbers tend to dominate the signal for systems with a source at redshift higher than 0.5.

The preliminary conclusion that the lensing distortions are dominated by line-of-sight haloes is encouraging because it greatly simplifies the theoretical analysis. Unlike for subhaloes, whose mass function is affected by environmental effects, calculating the mass function of dark central haloes in the mass range of interest - below the threshold for star formation - is straightforward since these haloes have never been affected by baryons. Thus, a standard calculation of the mass function based on dark-matter-only simulations (Frenk et al. 1988) gives very precise results (see Zavala & Frenk 2019, for a recent review).

By contrast, the mass function of subhaloes is determined by a number of processes, such as tidal stripping or tidal shocking, that alter the mass distribution and can destroy the subhalo. To calculate these processes requires modelling the host galaxy in detail, including its baryonic components. This is, of course, a much more complicated problem than simply following the evolution of dark matter haloes. Significant advances, however, have been achieved in recent years with a new generation of cosmological hydrodynamics simulations that can produce realistic galaxy populations (e.g. Vogelsberger et al. 2014; Schaye et al. 2015). Here, we will make extensive use of the high-resolution hydrodynamics simulation of

Richings et al. (2021) of a galaxy cluster and its environment which includes the relevant baryon physics processes.

Li17 and D18 both made an important assumption: that the perturbation induced by a subhalo can always be well fitted by the perturbation induced by a line-of-sight halo with an NFW profile. This assumption, however, may not be exactly true because the deflection angles produced by a line-of-sight halo can be very different from that of a subhalo in certain redshift ranges. Furthermore, these earlier studies did not carry out complete modelling of the lensing process, for example, assuming realistic noise levels, and this may further bias the results.

In this paper, we revisit the importance of the contribution of line-of-sight perturbers by modelling a set of realistic strong lensing mock images. In earlier studies, the comparison of deflection angles was used to decide whether a perturber is detectable or not, through the concept of an “effective mass”. Here we derive the detectable mass threshold for line-of-sight perturbers by directly evaluating the difference in log-likelihood between a model with a perturber and a model without a perturber, using a state-of-the-art strong lens modelling pipeline PyAutoLens¹ (Nightingale et al. 2018; Nightingale et al. 2021b). The new threshold is now directly obtained from modelling image fluxes and thus it is more straightforward and robust, where it takes into account factors from flux modelling processes previously not considered, like the degeneracy between the perturber and the macro model. We also investigate the dependence of the relative contribution of the two types of object on the redshift and the S/N ratio of the observations.

An independent study of the sensitivity function using PyAutoLens is provided by Amorisco et al. (2022). This work reassuringly reaches the same conclusion as us on the dependence of the sensitivity function on the redshift of the perturbing halo, despite using a different approach to calculate the sensitivity function and mock strong lens datasets with different properties. Looking at only line-of-sight haloes, this study highlights the impact that the intrinsic scatter in halo concentrations has on the sensitivity function, and shows that the dependency of the concentration–mass relation on the dark matter model improves strong lensing as a probe of dark matter. In this work, we explicitly include subhalos within the lens galaxy (in addition to line-of-sight haloes), accounting for their different mass function and density profiles due to baryonic physics. Thus, we set out to answer whether the line-of-sight or lens galaxy subhalos dominate the constraints on DM.

The structure of the paper is as follows. In Section 2, we describe how we construct mock lenses, how we compute the sensitivity map and the method we use to translate sensitivity maps into constraints on the halo mass function. In Section 3, we present our results and in Section 4, we summarize our conclusions. Throughout the paper we adopt the Planck cosmological parameters (Planck Collaboration et al. 2016): $H_0 = 67.7 \text{ km s}^{-1} \text{ Mpc}^{-1}$, $\Omega_m = 0.307$ and $\Omega_\Lambda = 0.693$.

2 METHOD

2.1 Mock Lenses

We construct five sets of mock lenses, including examples with different image configurations, redshifts, noise levels and angular

¹ <https://github.com/Jammy2211/PyAutoLens>

resolution. For simplicity we set the density distribution of all primary lenses to be singular isothermal ellipsoids (SIE),

$$\Sigma(x, y) = \frac{c^2}{8\pi G} \frac{D_A(0, z_s)}{D_A(z_1, z_s) D_A(0, z_1)} \frac{R_E}{\sqrt{x^2 q + y^2/q}}, \quad (1)$$

where R_E and q are the Einstein radius and axis ratio of the lens galaxy; $D_A(z_1, z_2)$ is the angular diameter distance between redshifts, z_1 and z_2 . The lens and source redshifts are marked as, z_1 and z_s , respectively. We do not add external shear in the mock lenses. However, when modelling the lens we do include the external shear as part of our mass model (Witt & Mao 1997).

To simulate the source galaxies, we assume a “cored” Sersic density profile:

$$I(r) = I' \exp \left[-b_n \left(\frac{r^\alpha + r_c^\alpha}{r_e^\alpha} \right)^{1/(n\alpha)} \right], \quad (2)$$

where I' is the scale intensity, r_e the effective radius, n the Sersic index and b_n a coefficient related to the Sersic index (see Eq. A7 of Trujillo et al. 2004). Compared to the standard Sersic profile, the core model introduces two additional parameters, r_c , which describes the core size, and α , which controls how fast the profile approaches constant surface brightness inwards. Throughout our tests we fix $\alpha = 2.0$ and $r_c = 0.01''$. The small core in our model helps to remove potential numerical inaccuracies induced by the cuspy nature of the regular Sersic profile.

The fiducial mock image setup has a nearly complete Einstein ring with the lens galaxy at redshift, $z = 0.5$, and the source galaxy at $z = 1$. The emission of the lens galaxy is omitted in this work. The mock image has similar angular resolution to HST imaging, where the pixel size is $0.05''$ and a Gaussian Point Spread Function (PSF) is assumed where $\sigma = 0.05''$ (FWHM of $\sim 0.118''$). For the noise level, we try to set it to be similar to the best cases in the SLACS sample (Bolton et al. 2006), where the maximum S/N in the image pixels is around 40 for a 2000s exposure. We adopt a background sky noise level of $0.1 \text{ e}^- \text{ pix}^{-1} \text{ s}^{-1}$, which is estimated from HST images of SLACS lenses. To add noise to each mock image, the background sky is added to the lensed source image, the data is converted to units of counts and Poisson noise values are drawn and added to every pixel. The source intensity is adjusted to make the maximum pixel S/N be ~ 40 and the data is then converted back to $\text{e}^- \text{ s}^{-1}$. The lens and source parameters of the fiducial setting is shown in the third column of Table 1.

Based on this fiducial setup, we also change the appropriate parameters to explore the effects of different image configurations, lens galaxy redshifts, noise levels and angular resolution. We summarize our mock images (without adding any low mass haloes) in Fig. 1, where each setting’s name is labelled in the upper left of each panel. The details of each setting are as follows:

- ER-EXP2000 — This is our fiducial setting, a nearly complete Einstein ring with a radius of $1.5''$, corresponding to an Einstein mass of $6.4 \times 10^{11} \text{ M}_\odot$ within 9.4 kpc.
- ER-EXP8000 — It has the same setting as our fiducial mock except the exposure time increases to 8000s, of which the maximum pixel S/N is ~ 80 .
- ER-EXP2000-LOWZ — The main lens in this case is located at redshift, $z = 0.22$, while the source is still at $z = 1$. When changing the lens redshift, we keep its Einstein radius (in arcsec) and noise level unchanged. At this redshift, a $1.5''$ Einstein radius corresponds to an Einstein mass of $1.3 \times 10^{11} \text{ M}_\odot$ within 5.5 kpc.
- QUAD-EXP2000 — In this setting, we simulate an image with quadruple arcs with the same noise level and angular resolution as

		Einstein Ring	Quad
Lens	(x, y) [“, “]	(0.0, 0.0)	(0.0, 0.0)
	$R_E ["]$	1.5	1.5
	q	0.95	0.65
	$\theta [^\circ]$	30	30
External Shear	magnitude	0.0	0.0
	$\theta [^\circ]$	0.0	0.0
Source	(x, y) [“, “]	(0.1, 0.1)	(-0.05, 0.1)
	$r_e ["]$	0.2	0.2
	q	0.52	0.7
	$\theta [^\circ]$	30	30
	$I' [\text{e}^- \text{ pix}^{-1} \text{ s}^{-1}]$	2.2	2.3
	n	2.5	2.0
	$r_c ["]$	0.01	0.01
	α	2.0	2.0

Table 1. Parameters of the lens and source galaxies for the Einstein Ring and Quad images in our mock simulations.

the fiducial case. The lens and source parameters of this configuration are listed in the fourth column of Table 1.

• ER-CSST — We also simulate a configuration with lens and source properties as in the fiducial case but with the same image resolution as the China Space Station Telescope (CSST). The CSST resolution is slightly worse than for the HST, with a pixel size of $0.075''$ and a PSF σ of $0.08''$ (FWHM of $\sim 0.188''$). We note that the hardware design of the CSST is not fully determined yet, so for our purpose here, which is to study purely resolution effects, we assume it has similar noise conditions as the HST except for the resolution. Since the pixel area is 2.25 times larger, the background sky noise is also increased to $0.225 \text{ e}^- \text{ pix}^{-1} \text{ s}^{-1}$. The image simulated here may therefore be treated as a pixel binned version of the fiducial mock image using a larger pixel and PSF size of the CSST.

• ER-JWST — The image resolution of this case is close to that of James Webb Space Telescope (JWST) images, which have a pixel size of $0.03''$ and a PSF σ of $0.013''$ (FWHM of $\sim 0.03''$). Note that now the pixel areas are 0.36 times those of the previous case; the noise is also changed consistently to be $0.036 \text{ e}^- \text{ pix}^{-1} \text{ s}^{-1}$.

In Table 2 we summarize the key features of the five mock settings (the quantities of the last three columns are defined in our results part, Sec. 3).

We perturb the images of the mock lenses with two types of objects. One are small-mass dark matter haloes along the line-of-sight and the other are subhaloes within the host halo of the lens galaxy. We model the line-of-sight haloes with spherical NFW profiles using the mass-concentration relation given by Ludlow et al. (2016), which has been shown to match the simulation data very well at the low mass end (Wang et al. 2020).

For subhaloes associated with the lens, their mass profile in the outer parts is modified by environmental effects such as tidal stripping. N-body simulations have shown that the density of these subhaloes drops dramatically beyond a truncation radius (e.g. Gao et al. 2004). In this paper we simulate the subhalo profile using a truncated NFW (tNFW) profile (see Eq. A.26~A.33 of Baltz et al. 2009),

$$\rho(r) = \frac{m_0}{4\pi} \frac{1}{r(r+r_s)^2} \left(\frac{r_t^2}{r_t^2+r^2} \right)^2, \quad (3)$$

where m_0 is the scale mass, r_s is the scale radius and r_t is the

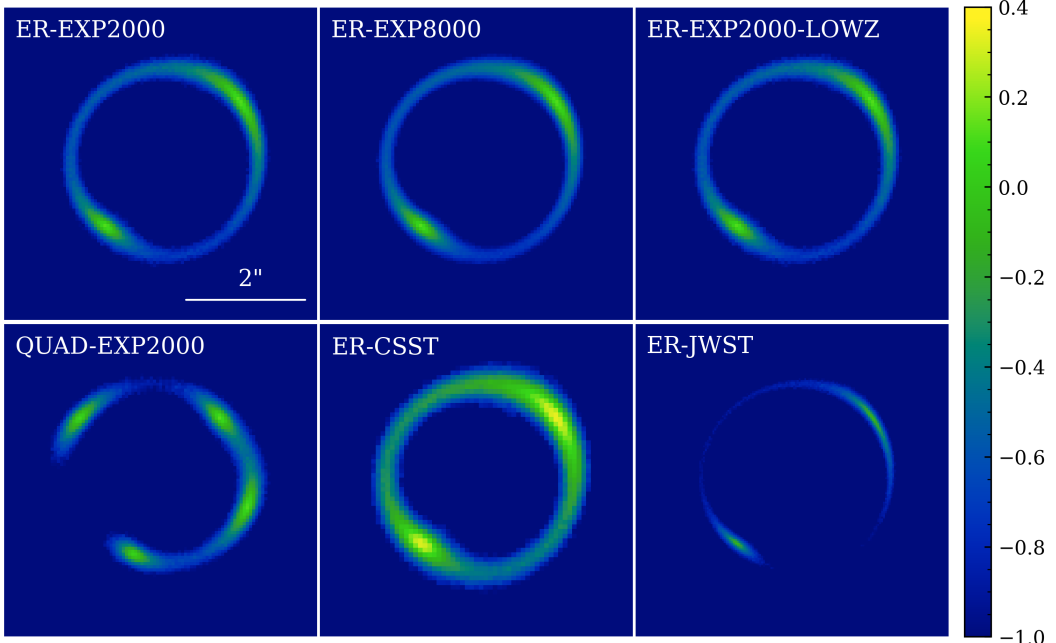


Figure 1. Mock observations of the galaxy-galaxy strong lens systems that we investigate. The name of each setting is shown on the top left of each panel. "ER-EXP2000" is our fiducial mock image. "ER-EXP8000" has a 8000s exposure. "ER-EXP2000-LOWZ" has a main lens located at $z = 0.22$. "QUAD-EXP2000" is an image with quadruple arcs. "ER-CSST" uses the resolution of CSST, which has a pixel size of $0.075''$ and a PSF sigma of $0.08''$ (FWHM of $0.188''$). "ER-JWST" uses the resolution of JWST, which has a pixel size of $0.03''$ and a PSF sigma of $0.013''$ (FWHM of $0.03''$). Parameters of the lens and source parameters for the Einstein Ring and Quad images are listed in Table 1. The key features of the systems are listed in Table 2. The images are shown in \log_{10} scale, and the unit of the color bar is $e^- \text{ pix}^{-1} \text{ s}^{-1}$.

Label	Configuration	z_l	z_s	Exposure time (s)	σ_{PSF}	Pixel size	N_{los}	N_{sub}	$N_{\text{los}}/N_{\text{sub}}$
ER-EXP2000	Einstein Ring	0.5	1.0	2000	0.05	0.05	0.85	0.66	1.29
ER-EXP8000	Einstein Ring	0.5	1.0	8000	0.05	0.05	2.50	1.24	2.02
ER-EXP2000-LOWZ	Einstein Ring	0.22	1.0	2000	0.05	0.05	0.39	0.38	1.03
QUAD-EXP2000	Quad	0.5	1.0	2000	0.05	0.05	0.64	0.51	1.25
ER-CSST	Einstein Ring	0.5	1.0	N.A. ¹	0.08	0.075	0.72	0.60	1.20
ER-JWST	Einstein Ring	0.5	1.0	N.A. ¹	0.03	0.03	1.06	0.75	1.41

¹ For our purpose to investigate how image resolution affect our results, we set them to have equivalent depth of observation as our fiducial setting.

Table 2. Column 1 shows the label of six mocks. Column 2-6 show the settings of lens configuration, including lens redshift, source redshift, exposure time, PSF size and pixel size. Column 7-8 show the expected detection of line-of-sight haloes, the subhaloes per system, and Column 9 shows the their ratio. Parameters of the Einstein Ring and Quad lens configurations are listed in Table 1.

truncation radius. The total mass of the subhalo, m_{tot} , can be written as (Eq. A.29 of [Baltz et al. 2009](#)),

$$m_{\text{tot}} = \frac{m_0 \tau^2}{2 (\tau^2 + 1)^3} \left[2\tau^2 (\tau^2 - 3) \ln \tau - (3\tau^2 - 1) (\tau^2 + 1 - \tau\pi) \right], \quad (4)$$

where $\tau \equiv r_t/r_s$.

We derive the mean relation between r_s , r_t and m_{tot} using the high-resolution hydrodynamical simulation by [Richings et al. \(2021\)](#). This is a zoom, high resolution resimulation of a halo with m_{200} (the mass within r_{200} , the radius where the enclosed density is 200 times the critical density of the Universe) of $10^{13.1} M_\odot$ at $z =$

0.18 selected from the [EAGLE](#) simulation volume ([Schaye et al. 2015](#)) and resimulated with 17 times better gas mass resolution than [EAGLE](#), $m_g = 1.8 \times 10^5 M_\odot$, and about 100 times better dark matter mass resolution than [EAGLE](#), $m_{\text{DM}} = 8.3 \times 10^4 M_\odot$. Such high resolution allows us to resolve the internal structure of subhaloes more massive than $10^8 M_\odot$. Haloes were identified using the friends-of-friends algorithm ([Davis et al. 1985](#)) and subhaloes using the [SUBFIND](#) algorithm ([Springel et al. 2001](#)); the density profiles of subhaloes in the mass range $10^8 \sim 10^{11} M_\odot$ were fit with the tNFW formula to derive the values of r_s , r_t and m_{tot} .

Since in actual observations, only subhaloes around the Einstein radius matter, we only select subhaloes whose projected posi-

tions fall in an annular region between $0.5''$ and $3.0''$ from the lens centre to derive the relations between r_s , r_t and m_{tot} . To improve the statistics, we rotated the simulated halo 10000 times at random. For the mock lenses at $z = 0.22$ and $z = 0.5$ we make use of the snapshots at $z = 0.183$ and $z = 0.503$ respectively. To make sure the derived relations are not dominated by any particular subhalo, e.g. by one very close to the Einstein radius in 3D, we carry out bootstrap tests whereby we repeat the same procedure 200 times and each time we derive the linear relations from a random re-sample of all subhaloes. The linear relation is computed by minimizing a χ^2 defined as:

$$\chi^2 = \sum_{i=1}^N W_i (y_i - (m \times x_i + c))^2, \quad (5)$$

where m , c are the linear relation slope and intercept, (x_i, y_i) is the coordinate of the i -th data point and W_i is the number of times the i -th data point is repeated in the sample. We then take the median linear relations from the 200 tests to model the subhaloes.

Taking the snapshot at $z = 0.183$ as an example, in Fig. 2, we plot the values of m_{tot} , r_s and τ (r_t/r_s) for subhaloes as blue circles. The area of each circle reflects how many times each subhalo fell on the annular region around the Einstein radius, which is taken as a weight for the point when deriving the linear relation. For this lens system we find,

$$\begin{aligned} \log_{10} \left(\frac{r_s}{\text{kpc}} \right) &= (0.60 \pm 0.09) \log_{10} \left(\frac{m_{\text{tot}}}{\text{M}_\odot} \right) - (4.85 \pm 0.77) \\ \log_{10} (\tau) &= (-1.21 \pm 0.10) \log_{10} \left(\frac{r_s}{\text{kpc}} \right) + (0.59 \pm 0.04). \end{aligned} \quad (6)$$

For the lens at $z = 0.5$ we find,

$$\begin{aligned} \log_{10} \left(\frac{r_s}{\text{kpc}} \right) &= (0.49 \pm 0.06) \log_{10} \left(\frac{m_{\text{tot}}}{\text{M}_\odot} \right) - (3.90 \pm 0.54) \\ \log_{10} (\tau) &= (-1.21 \pm 0.09) \log_{10} \left(\frac{r_s}{\text{kpc}} \right) + (0.55 \pm 0.03), \end{aligned} \quad (7)$$

where the errors are the 1σ scatter determined from the bootstrap resampling.

In Fig. 3, we show the interior mean surface density profiles of tNFW subhaloes of mass $m_{\text{tot}} = 10^9 \text{ M}_\odot$ for two different lens redshifts, and the same profiles of central haloes of mass $m_{200} = 10^9 \text{ M}_\odot$ for two different lens redshifts. The profiles of the tNFW model were derived from the mean linear relations between m_{tot} , r_s , and r_t described above. Clearly, the tNFW profiles are more compact and have higher amplitude than the NFW profiles of the same mass.

2.2 Sensitivity Mapping

A process called sensitivity mapping is performed to quantify the detectability of a perturbing halo that is nearby a strongly lensed source. One begins by modeling a strong lens dataset to infer an accurate model for the lens's mass and source's light (Nightingale et al. 2019). Using this model, one can then simulate a new realization of the strong lens which includes a dark matter perturber at a given (x, y) position in the image-plane and with an input mass and redshift. This simulated dataset assumes the same image resolution and PSF of the true dataset and also has consistent signal-to-noise properties.

The mock dataset is now fitted with two lens models: (i) a lens mass model which does not include a dark matter perturber

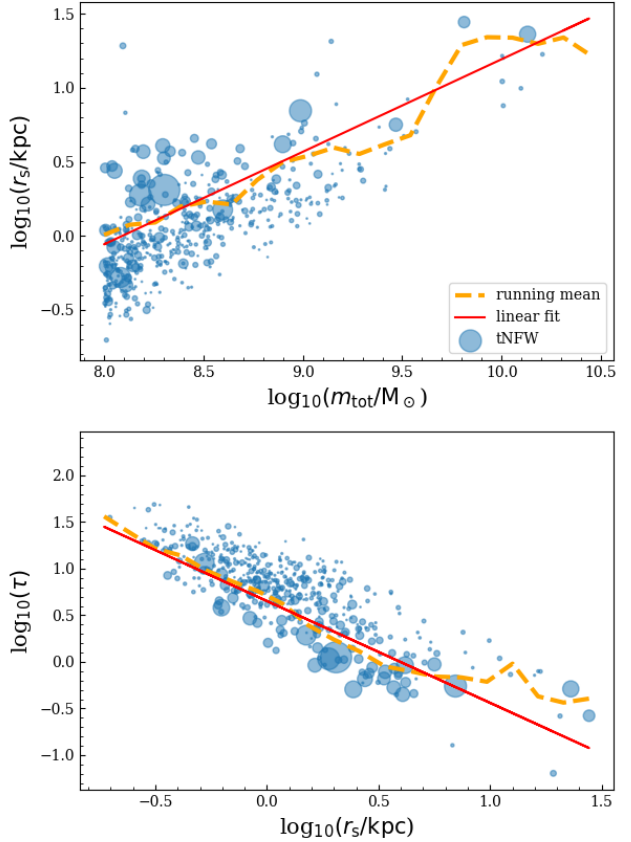


Figure 2. Relations between m_{tot} , r_s and τ for subhaloes in an annulus between $1.0''$ and $3.0''$ encompassing the Einstein radius, at snapshot $z = 0.183$. The relations were obtained by rotating the lensing galaxy and its subhaloes 10000 times and selecting those subhaloes that fall in the region of interest in projection. The area of each blue point represents how many times a subhalo falls in this region. The dashed orange and solid red lines show the running means and best fit linear relations for the data taking account of the weight of each data point.

and; (ii) a lens mass model which does. By comparing a goodness-of-fit measure of each model-fit (e.g. the maximum log likelihood value) one therefore quantifies how sensitive the lens dataset is to a dark matter perturber, given its input location and mass. If the lens model including the perturber has a much improved goodness-of-fit compared to the model which does not, the perturber was necessary to fit the data accurately, indicating that the strong lens data is sensitive to perturbers at the location and with that mass. If the goodness-of-fits are comparable, the perturber does not improve the lens model and therefore it is too far from the lensed source or too low mass to be detectable.

It is necessary to perform two full fits to each mock dataset, to infer the maximum log likelihood of each model, for two reasons. First, the image fluxes we are fitting have noise and thus the maximum likelihood model may not be the true input model (although see Amorisco et al. 2022). Second, due to the existence of a small perturber in the mock data and the possible degeneracy between it and the main lens mass, when fitting a model without a small perturber, the maximum likelihood model is offset with respect to the true input and can only be found via a full fit.

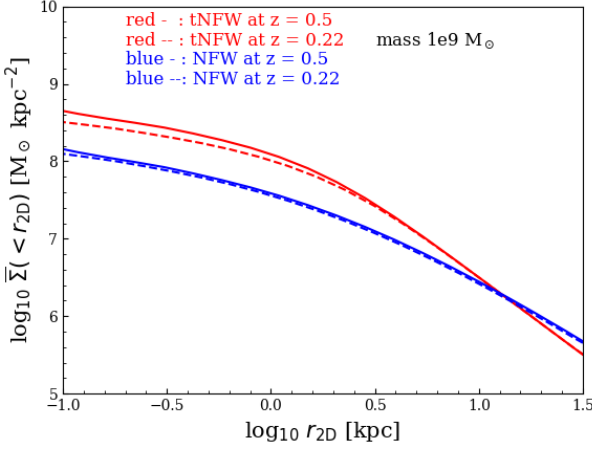


Figure 3. Interior mean surface density profiles of tNFW and NFW at $z = 0.22$ (dashed lines) and $z = 0.5$ (solid lines). Red lines are the tNFW profiles and blue lines show the NFW profiles. All the haloes plotted here have mass of $10^9 M_\odot$. For tNFW, the mass refers to the total mass, while for NFW, the mass refers to m_{200} .

By repeating this process on a grid of perturber (x, y) location, mass and redshift one produces a sensitivity map. In this work, we assume a grid of 27 steps in the y and x directions, and a grid of 25 steps in redshift between $z = 0.02$ and $z = 0.98$. For a given object, its angular size decreases with redshift, so the angular size of the sensitive region also decreases with redshift. To save computational resources, we decrease the angular size of the explored region as the redshift increases. Furthermore, for the same reason, rather than exploring a grid of mass values, we look for the lowest value of the perturber’s mass that corresponds to the goodness-of-fits threshold of detection by a binary search algorithm (in \log_{10} scale). The mass boundaries for the binary search are $10^6 M_\odot$ and $10^{11} M_\odot$ and the stop criterion for the iteration is that $|\Delta \log_{10}(m)| < 0.01$. For every grid cell, we simulate a new strong lens dataset and fit it with the two lens models described above using the nested sampling algorithm `dynesty` (Speagle 2020). For efficiency, we use tight priors on every model-fit that exploit our knowledge of what values of lens mass model and source model were used to when simulating the data. This could negatively impact `dynesty`’s estimate of the Bayesian evidence, therefore we opt to simply compare maximum log likelihood values when producing a sensitivity map. At the end, the “sensitivity map” is a grid of $(x_p, y_p, z_p, m_{\text{th}})$, which means that a perturber at (x_p, y_p, z_p) is detectable when it has a mass over the threshold mass, m_{th} . Please note when fitting the mock image with a lens mass model including a perturber model, the perturber model’s redshift is fixed to be z_p while its position and mass are free (the concentration follows Ludlow et al. (2016) which is a function of m and z_p). Fig. 4 summarizes the procedure of computing m_{th} for at (x_p, y_p, z_p) . Our method is conceptually analogous to that of Amorisco et al. (2022), albeit there are differences in the fitting algorithm used.

2.3 Detection threshold

Previous studies (Li et al. 2016; Despali et al. 2018) have derived the detection threshold of a line-of-sight perturbing halo by directly modelling the lensing effect of a subhalo, i.e. a perturber at the

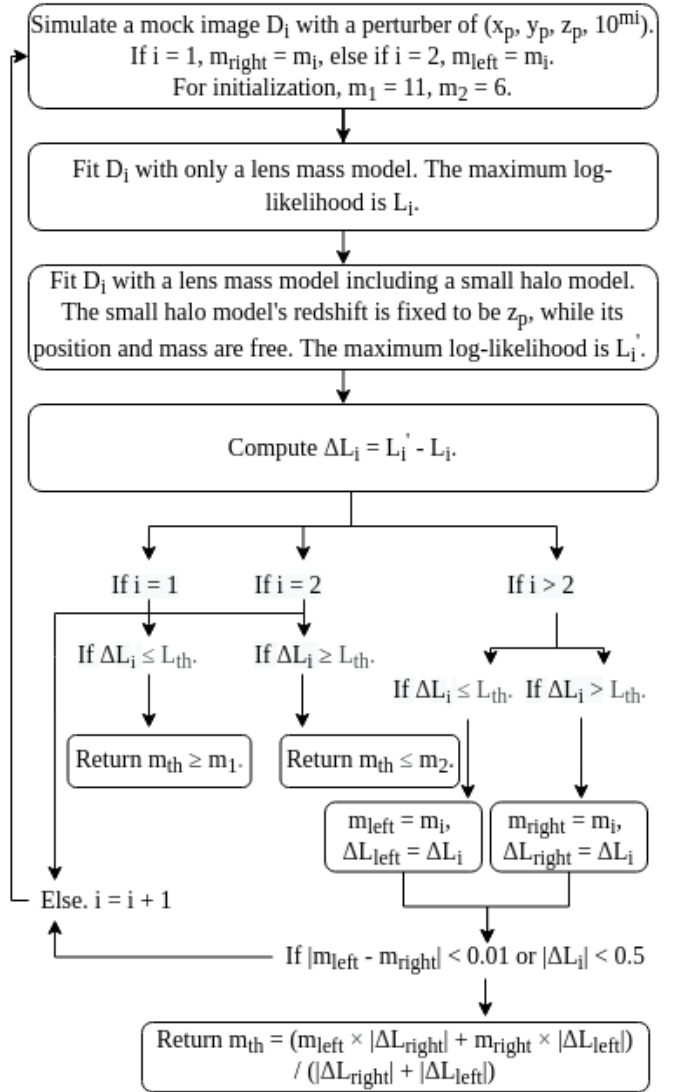


Figure 4. The binary search procedure for m_{th} at (x_p, y_p, z_p) . L_{th} is the detection threshold and throughout this paper, we take it to be 10.

redshift of the lens. If a line-of-sight halo of mass, m , best fits the lensing effect of a subhalo of mass, m_{sub} , then this is defined as the effective mass of the line-of-sight halo. If a line-of-sight halo has an effective mass larger than the detection threshold for the subhalo, it is considered detectable. However, in many cases, the line-of-sight halo at redshift z is not a good description of the image perturbation. As a result, although one can always find a particular value of m for a line-of-sight halo that gives the smallest χ^2 in the fit of the image distortion generated by the subhalo, the two models are not equivalent.

In Fig. 5, we show how the deflection angles produced by our lens are altered by the addition of a perturbing halo. The main lens is an singular isothermal sphere (SIS) located at $z = 0.5$, at the centre of the image, and the source is at $z = 1.0$. The upper panel shows the deflections caused by a $m_{200} = 10^9 M_\odot$ NFW halo located on the main lens plane; the colour indicates the amplitude of the deflections (in units of $0.001''$) and the arrows mark their directions. In this case there are no non-linear multi-plane lensing effects, and so the change in the deflection angles due to a perturbing halo are

just the deflection angles of the perturbing halo itself, which point towards the perturber's centre. In the lower panel we plot the change in the total deflection angles when a $m_{200} = 10^{8.67} M_{\odot}$ NFW halo at $z = 0.2$ perturbs the lensing due to the main lens (subtracting the total deflection angle with the deflection caused only by the main lens). Because of multi-plane lensing effects (Schneider et al. 1992; Fleury et al. 2021) the change in the deflection angles are no longer isotropic about the perturber centre (Gilman et al. 2019; He et al. 2022). Tracing from the observer backwards, the deflection of light rays by the perturber alters where those rays intersect the main lens plane, which in turn alters the deflection angles those rays receives from the main lens. It is clear that the lensing effects of line-of-sight perturbers at different redshifts cannot be reproduced by appropriately scaled subhaloes since the deflection patterns in the two cases are completely different. Note that the mass of the line-of-sight perturber in the lower panel was chosen to best reproduce the deflection angle field in the annulus between $1.0''$ to $2.0''$ of the case in the top panel with a $10^9 M_{\odot}$ halo in the main lens plane (following Eq. 15 in D18), so according to Li17 and D18, the perturbers in the two panels have the same ‘‘effective mass’’, but clearly they have quite different effects.

Degeneracies between the effects of the low-mass perturber and the main lens can also affect our estimation. As suggested in Fig. 5, the deflection angles far from the perturber's centre can be easily absorbed by slightly shifting and stretching the main lens. Furthermore, the degeneracies between the effects of perturbers and the main lens galaxy can be different at different redshifts due to their distinct deflection patterns, making the problem even more complicated.

In order to take into full account the complex effects discussed above, in this paper we no longer compare deflection angles as Li17 and D18 did. Instead, to quantify the lensing effects of perturbers at different redshifts we directly fit image fluxes, a procedure that more closely reproduces what would happen on real data. We now define a new threshold for detection through the log-likelihood² improvement brought about by including a perturber when fitting lensing images. Specifically, we first fit the mock image with only a main lens and record the maximum log-likelihood value. We then fit the same image with a model containing both a main lens and a perturbing halo and record the log-likelihood of the best-fit model as well. If the log-likelihood difference between the two fits is larger than a pre-established threshold, we consider the perturber to be detectable.

In the tests we have carried out, the uncertainty in the modelling comes exclusively from the statistical noise in the image data. The log-likelihood difference can be directly related to a significance level, with a log-likelihood difference of 10 roughly corresponding to $4 \sim 5\sigma$ significance. Note that in real observations, a threshold based on the log-likelihood difference or the Bayesian evidence might not be readily related to the true significance of a detection due to the possible presence of various systematic effects in the data and analysis method (Vegetti et al. 2012; Ritondale et al. 2019).

2.4 Number density of perturbers

For each mock lens, we calculate the number of line-of-sight perturbing haloes within a radius of 3 arcsec. The total number of

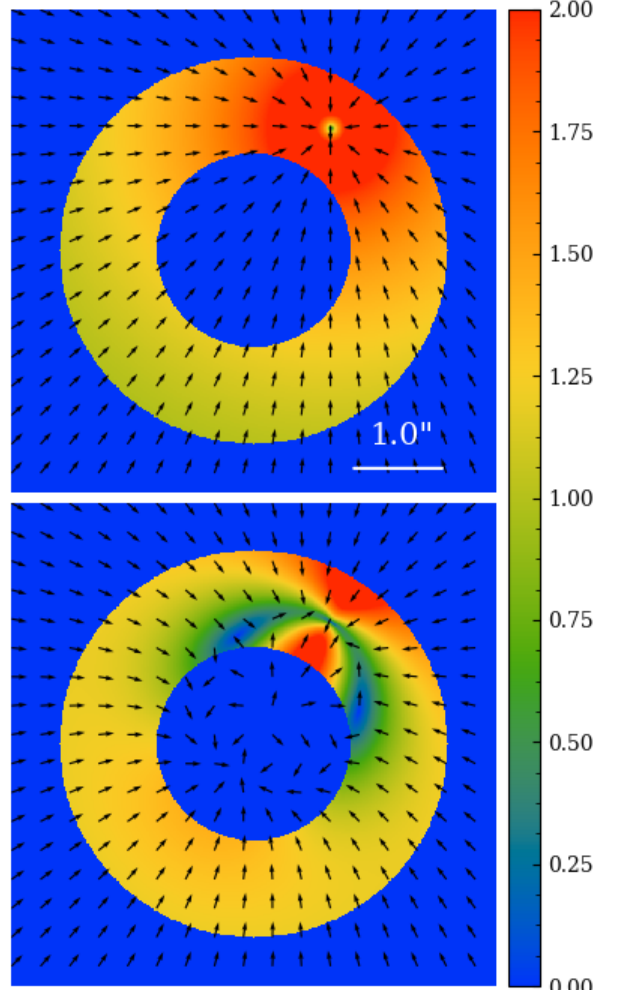


Figure 5. Comparison of the deflection angles caused by a $10^9 M_{\odot}$ NFW halo at lens plane ($z = 0.5$) (upper panel) and a line-of-sight NFW halo in front of the lens plane ($z = 0.2$) whose mass is $10^{8.67} M_{\odot}$, as derived by fitting the deflection angle of the NFW halo at the main lens plane (lower panel). Both panels are derived by subtracting the total deflection angles of both main lens and perturber with the deflection generated only by the main lens. The colours show the amplitude of deflections (in units of $0.001''$). The arrows represent the direction of deflection angle vectors. In the lower panel, the asymmetric pattern of arrows at the centre of the main lens is subject to numerical noise because the deflection angle at the exact centre of an SIS is not well defined, where the profile's density is infinite and the density gradient (deflection angle) is not continuous. Since the perturber and the SIS are not on the same plane in the lower panel case, the inaccurate angles next to the SIS's centre are then not perfectly subtracted, which results in the asymmetric pattern of arrows in the centre. The arrows in other locations are reliable.

line-of-sight perturbers with a mass in the range $[m_{\text{low}}, m_{\text{high}}]$ in a light cone corresponding to the i^{th} pixel can be written as,

$$N_{\text{los}} = \int_0^{z_s} \int_{m_{\text{low}}}^{m_{\text{high}}} \frac{d^2 N}{dm dV} \frac{dV_{\text{sens}}}{dz} dm dz, \quad (8)$$

² The log likelihoods are defined using a natural (base e) logarithm.

where $\frac{d^2N}{dm dV}(z)$ is the halo mass function at redshift z (e.g. Sheth et al. 2001) and

$$dV_{\text{sens}} = \Omega_{\text{sens}}(m, z) \chi^2 \frac{d\chi}{dz} dz, \quad (9)$$

where $\Omega_{\text{sens}}(m, z)$ is the total solid angle corresponding to the areas on the redshift plane of z that are sensitive to perturbers more massive than m .

For comparison, we also calculate the number of detectable subhaloes for each mock image. For CDM, high-resolution N-body simulations have shown that the mass function of subhaloes follows a power law (Springel et al. 2008). Thus, the cumulative perturber density of subhaloes in the mass range, $[m_1, m_2]$, in a host halo of mass, m_{200} , may be written as,

$$\Sigma_{\text{sub, cdm}}(m_1 < m < m_2 | m_{200}) = \frac{\Sigma_0}{1 - \alpha} \left(\left(\frac{m_2}{M_\odot} \right)^{1-\alpha} - \left(\frac{m_1}{M_\odot} \right)^{1-\alpha} \right), \quad (10)$$

where $\alpha = 1.9$ (Springel et al. 2008; Gao et al. 2012) and Σ_0 is a normalization parameter that depends on m_{200} and can be determined from cosmological simulations. In this work, we estimate this normalization using the same simulation (Richings et al. 2021) that we used to extract the density structure of subhaloes.

To obtain a sufficiently large sample of subhaloes within the region of interest in order to derive the subhalo mass function, we follow the same strategy as before: we rotate the lens 10000 times, and only select those subhaloes that fall on the region of interest in projection. We compute the average number of subhaloes of mass $10^7 \sim 10^{11} M_\odot$ for each projection. To obtain an estimate on the error, we repeat the same procedure 200 times, each time resampling from all the subhaloes in the simulation before projecting along 10000 different lines-of-sight. We take the median value and 1σ limits as our estimate. Assuming $\alpha = 1.9$, for a lens at $z = 0.22$, we derive the normalization (from the snapshot at $z = 0.183$) to be $(6.7 \pm 0.6) \times 10^5 \text{ arcsec}^{-2}$. For a lens at $z = 0.5$, we derive the normalization (from the snapshot at $z = 0.503$) to be $(2.3 \pm 0.2) \times 10^6 \text{ arcsec}^{-2}$.

To ensure that our result based on this one particular simulated halo is not an outlier, we compute the normalisation of the subhalo mass function from haloes in the EAGLE simulation in a similar way as above. Due to the poorer resolution of EAGLE, when calculating the normalisation we only count subhaloes of mass $10^9 \sim 10^{11} M_\odot$. We select haloes in EAGLE with mass within 0.1 dex of that of the main halo used in this study and apply the same method to compute Σ_0 . For $z = 0.22$, there are 78 haloes and $\Sigma_0 = (4.3 \pm 1.5) \times 10^5 \text{ arcsec}^{-2}$, where the errors indicate the 1σ (34%) scatter. For $z = 0.5$, there are 63 EAGLE haloes and $\Sigma_0 = (1.8 \pm 0.9) \times 10^6 \text{ arcsec}^{-2}$. We see that the number of EAGLE subhaloes around halos of a given mass has a large scatter and there can be differences of $2 \sim 3$ times within EAGLE itself. At $z = 0.22$, the value of Σ_0 obtained for the halo analysed here is 1σ high compared to the distribution in EAGLE, while at $z = 0.5$, the results are in even better agreement. In conclusion, the value of Σ_0 derived in this work is comparable to values for EAGLE haloes and our results based on one particular resimulation should be representative.

3 RESULTS

In Fig. 6 we show the sensitivity function for our mock lens images as a function of redshift. Each sub-panel displays a map of m_{th} (see

colour bar) for line-of-sight haloes placed at a given redshift plane, for 5 redshifts. In all cases, the source is at $z = 1$ and the lens at $z = 0.5$, except in the third row, where the lens is at $z = 0.22$. For all mock lenses, the threshold mass of a detectable perturber is lowest near the lens redshift and raises rapidly towards both higher and lower redshifts; however, the general pattern of the sensitivity maps remains similar at each redshift. This pattern varies considerably from one lensing system to another. Visually, it appears similar to the corresponding pattern of the lensing image. The value of m_{th} is lowest in the region where the surface brightness is highest and highest in the region where there is no light. Although the sensitivity maps for different systems are quite different, the trend of their evolution with redshift is similar.

The ability to detect low-mass dark haloes increases significantly with the exposure time of the imaging. For our fiducial 2000s exposures, our lensing systems are sensitive to line-of-sight perturbers of mass $\sim 10^8 M_\odot$ only around the lens redshift. For 8000s, however, perturbers of mass $\sim 10^8 M_\odot$ can be detected over a much broader redshift range, from $z = 0.1$ to $z = 0.7$. In the bottom two rows of Fig. 6, we show the sensitivity function for the imaging quality achievable with the CSST and JWST, which have different resolutions. We find that with a lower image resolution, CSST lensing images are still sensitive to perturbers of mass $\sim 10^8 M_\odot$, although the overall sensitivity is somewhat lower than with HST resolution. While for the JWST resolution imaging, the sensitivity is higher.

We now turn our attention to the all-important question of whether the distortions to the Einstein rings are dominated by line-of-sight perturbers or by subhaloes. We trace the position of each pixel on the image plane at a series of redshifts and calculate the threshold mass for detection, $m_{\text{th}}(z)$. In Fig. 7, we plot the ratio, $\log_{10}(m_{\text{th}}(z)/m_{\text{th}}(z_1))$, as a function of redshift, z , for our different mock lensing systems. The colour bands are the regions enclosing 70% of the pixels, while the means are shown as solid lines. For comparison, we also plot the relation and scatter derived by D18 in grey. In D18 (as well as in Li17), a line-of-sight halo at lower redshift is easier to detect than a halo of the same mass at the lens redshift. Our new calculations predict the different behaviour. For all configurations, the detection threshold mass increases with $\Delta z = |z - z_1|$. For lenses at redshift $z_1 = 0.5$, the detection threshold for line-of-sight haloes at $z = 0.1$ is ~ 0.3 dex higher than for haloes at z_1 .

To predict the number density of detectable subhaloes, we calculate sensitivity maps for subhaloes with truncated NFW profiles, as described in Sec. 2.1. In Fig. 8, we compare sensitivity maps for subhaloes (right) to those for line-of-sight haloes placed at the lens redshift of the same lensing system (left). The maps on the left are the same as in the subpanels of Fig. 6 at the corresponding (lens) redshift, while the right panels show the detection limits for subhaloes. The mass of an NFW halo is defined to be m_{200} , while the mass of the subhalo (tNFW) is defined as the total mass given by Eq. 4. As expected, the threshold mass for detecting a subhalo is lower than that for detecting an NFW halo of the same mass by about 0.5 dex, because a subhalo is much more compact than a halo of the same mass. In the following calculations, we will use the sensitivity maps for the tNFW haloes to estimate the number of detectable subhalo perturbers.

In the left panel of Fig. 9, we show, as solid lines, the expected cumulative number of detectable line-of-sight perturbers derived, as a function of redshift; different colours correspond to different systems. We can see that the number of detections rises sharply around the lens redshift and then becomes flat. For the two different

mock lenses at $z_l = 0.5$, with a 2000s exposure (blue and green lines), 0.85 and 0.64 line-of-sight haloes can be detected per lens. The differences between the two configurations are small, which may be due to the fact that the two mock images have a similar number of high S/N pixels. For the lens at $z_l = 0.22$, the number of expected detections decreases to about 0.39 per lens (red line), which is $\sim 45\%$ of that of the $z_l = 0.5$ lenses. Fig. 9 also shows that a high S/N ratio (blue line) helps reveal low-mass perturbers: if the exposure time increases to 8000s, the number of detectable line-of-sight perturbers increases to 2.5 per lens. We also see that by increasing the image resolution, the detectability of small perturbers increases. With CSST resolution only ~ 0.72 line-of-sight perturber can be detected per lens, but with a higher resolution as the JWST, the detectable number increases to 1.06 per lens.

On the right panel of Fig. 9, we show the relative importance of line-of-sight haloes and subhaloes. According to our calculation, for mock lenses at $z_l = 0.5$, the predicted number of detectable line-of-sight haloes is about 1.3 times the number of detectable subhaloes. For the low redshift mock, $z_l = 0.22$, the line-of-sight halo contribution is lower and close to that of subhaloes. For the high S/N mock, the relative importance of line-of-sight haloes increases, such that it becomes ~ 2.0 times the number of detectable subhaloes.

4 DISCUSSION AND CONCLUSION

In this study we have revisited a key question relevant to the search for low-mass haloes in strong lensing systems: what is the relative contribution to the sensitivity function of line-of-sight (main) haloes versus subhaloes in the lens. The main difference between this and previous works is that, instead of fitting the deflection angle map or an idealized image set, we have quantified the expected number of line-of-sight perturbers by means of realistic modelling carried out with the PyAutoLens lensing package on a set of mock lensing images with realistic levels of noise. Contrary to previous work, we find that the lensing effect of a line-of-sight perturber is largest if the perturber is located near the lens redshift, and the strength of the signal decreases rapidly as the redshift difference between the perturber and the lens plane increases. Two reasons account for the difference: firstly, previous work assumed that the effects of a perturber at one redshift could be accounted for by a perturber at a different redshift, while Fig. 5 demonstrates that the effects can be quite different because of multi-plane lensing effects; secondly, previous work did not take into account the degeneracy between the main lens and the small halo in the fitting process, whereby changes to the main lens model can absorb a significant part of the small perturber's lensing signal. Our calculation shows that the contribution from line-of-sight haloes is still important, but does not dominate the total number of detectable perturbers for most of our mock lenses as was previously thought: previous studies overestimated the expected total number of perturbers.

In a sense, our new results present an unwanted challenge for the interpretation of future detections of low-mass haloes. Unlike the line-of-sight field dark matter haloes of interest (whose masses are below the minimum required to make a galaxy) which are unaffected by baryons and thus retain their pristine structure, subhaloes are changed by their environment, e.g. tidal striping and disruption. A detailed quantification of these processes needs understanding in detail the structure of the galaxy, including its baryonic component. This requires full modelling of galaxy formation such as that presented by Richings et al. (2020) for a lens system of the kind in which we are interested for low-mass halo and subhalo detection.

In this work we have assumed, for simplicity, that the distribution of line-of-sight haloes is not correlated with the lens host halo. In reality, line-of-sight haloes are more strongly, and anisotropically clustered around the region of the host halo than average (Richings et al. 2021). In a recent paper, Lazar et al. (2021) investigated the number density of line-of-sight perturbers in the simulations from the FIRE³ and IllustrisTNG⁴ projects; they find that the number of haloes correlated with the lens is about 35% larger than average, in agreement with the results of Richings et al. (2021). Future work aimed at constraining the nature of the dark matter from strong lensing data will need to take this sort of correlation into account.

One caveat of our work is that we do not consider the scatter in the mass-concentration relation. For a halo or subhalo of a given mass, the higher the concentration, the higher the central density and lensing signal. A recent study by Minor et al. (2021) shows that this effect can introduce a bias of 3 for a subhalo of mass $10^9 M_\odot$ and 6 for one of mass $10^{10} M_\odot$. In a more recent study, Amorisco et al. (2022) show that the scatter in the mass-concentration relation boosts the detection of line-of-sight perturbers and helps distinguish between CDM and WDM. A halo of mass less than m_{th} but of higher than average concentration may still produce a strong enough lensing signal to be detected and vice versa. When the halo or subhalo mass function rises at the low mass end, the effect of scatter in the mass-concentration relation can boost the number of detectable perturbers significantly, helping distinguish different dark matter models. We remind our readers that the results discussed here are for analyses of resolved lensing systems where the sources are extended. Effects of mass-concentration relation and multi-plane lensing have been taken into account in previous similar studies on constraining low-mass perturbers' abundance in lensing systems with an unresolved source (Gilman et al. 2019, 2020).

In this work, we also show that the ability to detect low-mass haloes increases with the exposure time of the image. For example, increasing the exposure time from 2000s to 8000s, increases the number of total detectable perturbers by a factor of 2. At face value, deeper imaging may seem not quite as efficient an observing strategy as observing more lenses. However, longer exposure times crucially increase the sensitivity to haloes of lower mass, which are important in constraining the identity of the dark matter.

SOFTWARE CITATIONS

This work used the following software packages:

- **Astropy** (Astropy Collaboration et al. 2013; Price-Whelan et al. 2018)
- **corner.py** (Foreman-Mackey 2016)
- **dynesty** (Speagle 2020)
- **Colossus** (Diemer 2018)
- **hmf** (Murray et al. 2013)
- **matplotlib** (Hunter 2007)
- **NumPy** (van der Walt et al. 2011)
- **PyAutoFit** (Nightingale et al. 2021a)
- **PyAutoLens** (Nightingale & Dye 2015; Nightingale et al. 2018; Nightingale et al. 2021b)
- **Python** (Van Rossum & Drake 2009)
- **Scipy** (Virtanen et al. 2020)

³ <http://fire.northwestern.edu>

⁴ <https://www.tng-project.org>

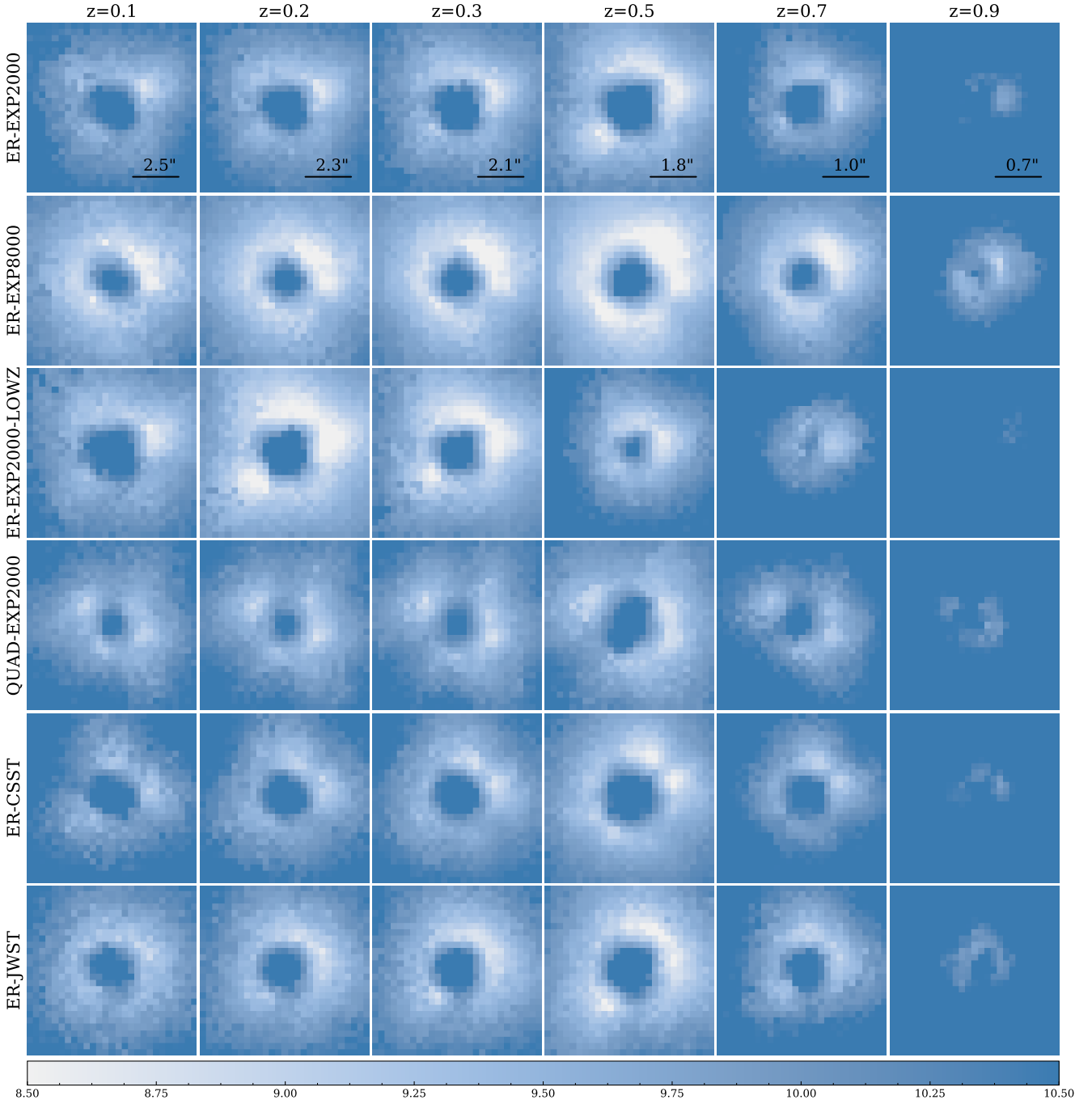


Figure 6. The sensitivity function of LOS perturbers. Each subpanel shows the detection limit for a perturber (a line-of-sight NFW halo) placed at a given redshift plane. The colour bar gives the scale of $\log_{10}(m_{\text{th}}/\text{M}_{\odot})$. 6 panels on the same row show the sensitivity function for a mock lens at 6 redshifts: 0.1, 0.2, 0.3, 0.5, 0.7, 0.9. For every column, the image size is marked by a scale bar in the top row. The label of each mock is given at the left of each row. In all cases the source is at $z = 1$ and the lens is at $z = 0.5$, except in the third row, where the lens is at $z = 0.22$. The image sizes decrease with the redshift because the angular size of regions of interests decreases with the redshift.

5 ACKNOWLEDGEMENTS

We thank the anonymous referee for insightful comments that helped us improve our paper. RL acknowledge the support of National Nature Science Foundation of China (Nos 11988101, 11773032, 12022306)), the science research grants from the China Manned Space Project (No CMS-CSST-2021-B01, CMS-

CSST-2021-A01), the support from K.C.Wong Education Foundation. QH, AA, CSF and SMC acknowledge support from the European Research Council (ERC) through Advanced Investigator grant DMIDAS (GA 786910). We also acknowledge support from the STFC Consolidated Grant ST/T000244/1. JWN and RJM acknowledge support from the UKSA through awards ST/V001582/1 and ST/T002565/1; RJM is also supported by the Royal Society. AR

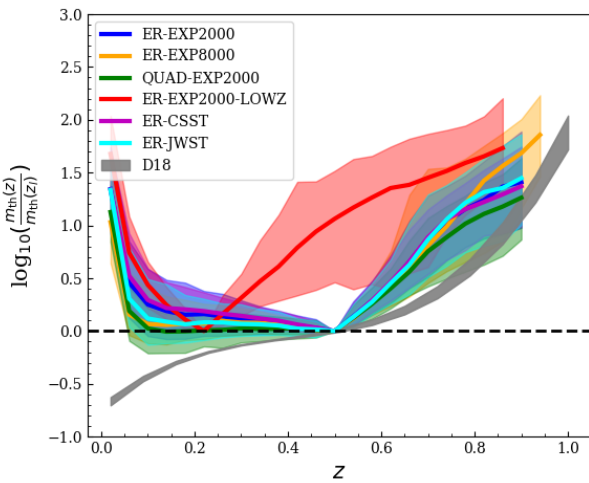


Figure 7. The mass threshold-redshift relation, $\log_{10} \left(\frac{m_{\text{th}}(z)}{m_{\text{th}}(z_l)} \right)$, as a function of redshift, z , for all of our mock settings. Four of them have a lens at $z = 0.5$ and a source is at $z = 1$, while one has a lens at $z = 0.22$. The relation is calculated for each pixel on the image plane. The shaded regions enclose 70% of the pixels. For comparison, the relation and the scatter derived by D18 for our fiducial setting are shown in grey. The relations shown here are only for line-of-sight NFW perturbers and there is no subhalo (tNFW perturbers) involved in this comparison.

is supported by the ERC through Horizon2020 grant EWC (AMD-776247-6). NCA is supported by an STFC/UKRI Ernest Rutherford Fellowship, Project Reference: ST/S004998/1. This work used the DiRAC@Durham facility managed by the Institute for Computational Cosmology on behalf of the STFC DiRAC HPC Facility (www.dirac.ac.uk). The equipment was funded by BEIS capital funding via STFC capital grants ST/K00042X/1, ST/P002293/1, ST/R002371/1 and ST/S002502/1, Durham University and STFC operations grant ST/R000832/1. DiRAC is part of the National e-infrastructure.

DATA AVAILABILITY

The data underlying this article will be shared on reasonable request to the corresponding author.

REFERENCES

- Amorisco N. C., et al., 2022, *MNRAS*, **510**, 2464
- Astropy Collaboration et al., 2013, *A&A*, **558**, A33
- Baltz E. A., Marshall P., Oguri M., 2009, *J. Cosmology Astropart. Phys.*, **2009**, 015
- Benitez-Llambay A., Frenk C., 2020, *MNRAS*, **498**, 4887
- Bolton A. S., Burles S., Koopmans L. V. E., Treu T., Moustakas L. A., 2006, *ApJ*, **638**, 703
- Bose S., Hellwing W. A., Frenk C. S., Jenkins A., Lovell M. R., Helly J. C., Li B., 2016, *MNRAS*, **455**, 318
- Boyarsky A., Ruchayskiy O., Iakubovskiy D., Franse J., 2014, *Physical Review Letters*, **113**, 251301
- Bulbul E., Markevitch M., Foster A., Smith R. K., Loewenstein M., Randall S. W., 2014, *ApJ*, **789**, 13
- Colín P., Avila-Reese V., Valenzuela O., 2000, *ApJ*, **542**, 622
- Davis M., Efstathiou G., Frenk C. S., White S. D. M., 1985, *ApJ*, **292**, 371

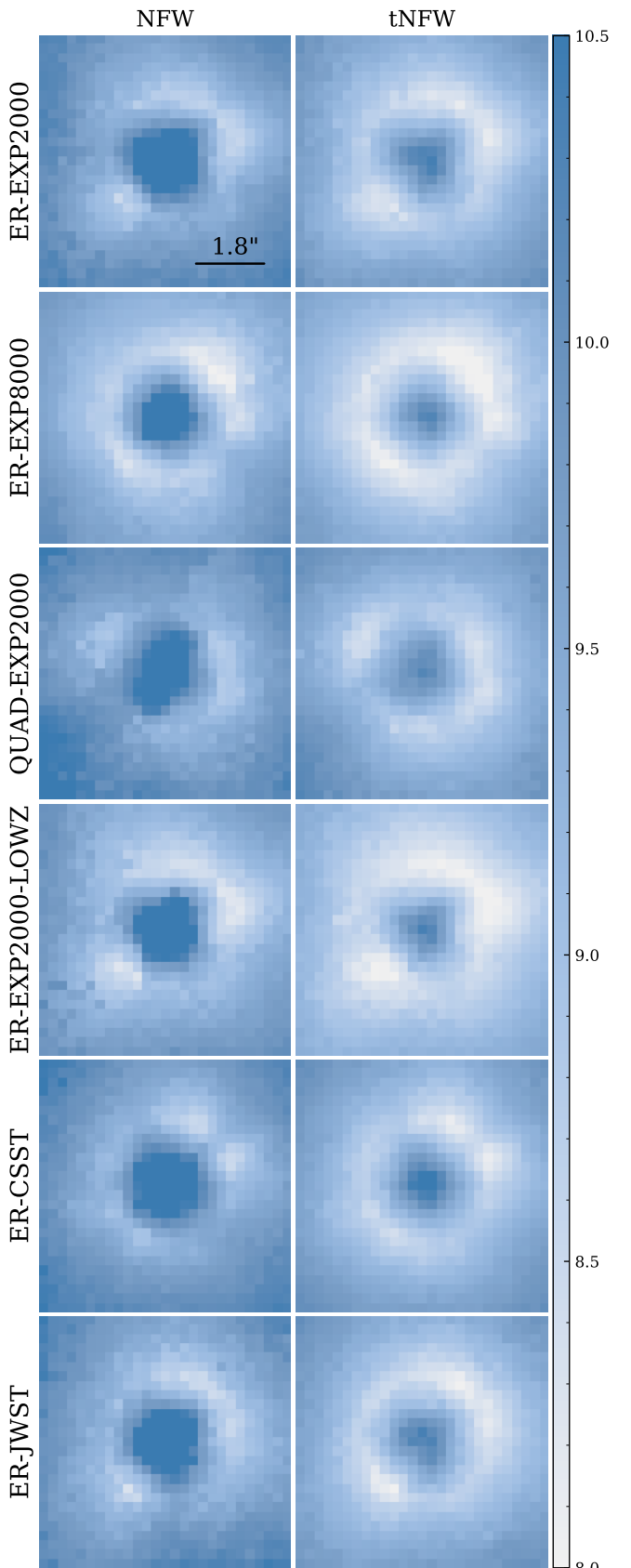


Figure 8. Sensitivity maps for NFW line-of-sight perturbers (left) and for tNFW subhalo perturbers (right). In all cases the source is at $z = 1$ and the lens at $z = 0.5$, except in the fourth row, where the lens is at $z = 0.22$. All perturbers are on the same redshift plane of the main lens.

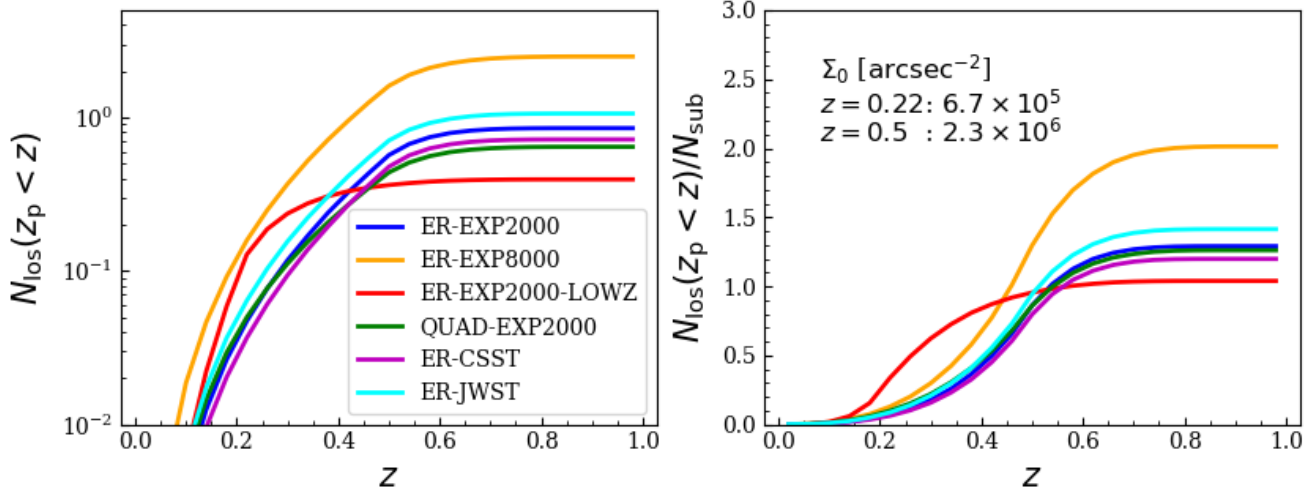


Figure 9. The cumulative number of detectable line-of-sight perturbers per lens for different lens configurations as a function of redshift (left). The number of line-of-sight haloes relative to the number of detectable subhaloes as a function of redshift (right). In all cases the source is at $z = 1$ and the lens at $z = 0.5$, except for the red line, where the lens is at $z = 0.22$. The normalization of the subhalo mass function at two main lens redshifts is also listed on the right panel.

Despali G., Vegetti S., White S. D. M., Giocoli C., van den Bosch F. C., 2018, [MNRAS](#), **475**, 5424

Diemand J., Kuhlen M., Madau P., 2007, [ApJ](#), **667**, 859

Diemer B., 2018, [The Astrophysical Journal Supplement Series](#), **239**, 35

Fleury P., Larena J., Uzan J.-P., 2021, [J. Cosmology Astropart. Phys.](#), **2021**, 024

Foreman-Mackey D., 2016, [The Journal of Open Source Software](#), **1**, 24

Frenk C. S., White S. D. M., 2012, [Annalen der Physik](#), **524**, 507

Frenk C. S., White S. D. M., Davis M., Efstathiou G., 1988, [ApJ](#), **327**, 507

Gao L., White S. D. M., Jenkins A., Stoehr F., Springel V., 2004, [MNRAS](#), **355**, 819

Gao L., Navarro J. F., Frenk C. S., Jenkins A., Springel V., White S. D. M., 2012, [MNRAS](#), **425**, 2169

Gilman D., Birrer S., Treu T., Nierenberg A., Benson A., 2019, [MNRAS](#), **487**, 5721

Gilman D., Du X., Benson A., Birrer S., Nierenberg A., Treu T., 2020, [MNRAS](#), **492**, L12

Green A. M., Hofmann S., Schwarz D. J., 2005, [J. Cosmology Astropart. Phys.](#), **8**, 003

He Q., et al., 2022, [MNRAS](#), **511**, 3046

Hezaveh Y. D., et al., 2016, [ApJ](#), **823**, 37

Hunter J. D., 2007, [Computing in Science & Engineering](#), **9**, 90

Koopmans L. V. E., 2005, [MNRAS](#), **363**, 1136

Lazar A., Bullock J. S., Boylan-Kolchin M., Feldmann R., Çatmabacak O., Moustakas L., 2021, [MNRAS](#), **502**, 6064

Li R., Frenk C. S., Cole S., Gao L., Bose S., Hellwing W. A., 2016, [MNRAS](#), **460**, 363

Li R., Frenk C. S., Cole S., Wang Q., Gao L., 2017, [MNRAS](#), **468**, 1426

Lovell M. R., et al., 2012, [MNRAS](#), **420**, 2318

Ludlow A. D., Bose S., Angulo R. E., Wang L., Hellwing W. A., Navarro J. F., Cole S., Frenk C. S., 2016, [MNRAS](#), **460**, 1214

Minor Q., Kaplinghat M., Chan T. H., Simon E., 2021, [MNRAS](#)

Murray S. G., Power C., Robotham A. S. G., 2013, [Astronomy and Computing](#), **3**, 23

Nightingale J. W., Dye S., 2015, [MNRAS](#), **452**, 2940

Nightingale J. W., Dye S., Massey R. J., 2018, [MNRAS](#), **478**, 4738

Nightingale J. W., Massey R. J., Harvey D. R., Cooper A. P., Etherington A., Tam S. I., Hayes R. G., 2019, [MNRAS](#), **489**, 2049

Nightingale J. W., Hayes R. G., Griffiths M., 2021a, [Journal of Open Source Software](#), **6**, 2550

Nightingale J. W., et al., 2021b, [Journal of Open Source Software](#), **6**, 2825

Planck Collaboration et al., 2016, [A&A](#), **594**, A13

Price-Whelan A. M., et al., 2018, [AJ](#), **156**, 123

Richings J., et al., 2020, [MNRAS](#), **492**, 5780

Richings J., Frenk C., Jenkins A., Robertson A., Schaller M., 2021, [MNRAS](#), **501**, 4657

Riemer-Sørensen S., 2016, [A&A](#), **590**, A71

Ritondale E., Vegetti S., Despali G., Auger M. W., Koopmans L. V. E., McKean J. P., 2019, [MNRAS](#), **485**, 2179

Sawala T., et al., 2016, [MNRAS](#), **456**, 85

Schaye J., et al., 2015, [MNRAS](#), **446**, 521

Schneider P., Ehlers J., Falco E. E., 1992, [Gravitational Lenses](#), doi:10.1007/978-3-662-03758-4.

Schneider A., Smith R. E., Macciò A. V., Moore B., 2012, [MNRAS](#), **424**, 684

Sheth R. K., Mo H. J., Tormen G., 2001, [MNRAS](#), **323**, 1

Speagle J. S., 2020, [MNRAS](#), **493**, 3132

Springel V., White S. D. M., Tormen G., Kauffmann G., 2001, [MNRAS](#), **328**, 726

Springel V., et al., 2008, [MNRAS](#), **391**, 1685

Trujillo I., Erwin P., Asensio Ramos A., Graham A. W., 2004, [AJ](#), **127**, 1917

Van Rossum G., Drake F. L., 2009, [Python 3 Reference Manual](#). CreateSpace, Scotts Valley, CA

Vegetti S., Koopmans L. V. E., 2009a, [MNRAS](#), **392**, 945

Vegetti S., Koopmans L. V. E., 2009b, [MNRAS](#), **400**, 1583

Vegetti S., Koopmans L. V. E., Bolton A., Treu T., Gavazzi R., 2010, [MNRAS](#), **408**, 1969

Vegetti S., Lagattuta D. J., McKean J. P., Auger M. W., Fassnacht C. D., Koopmans L. V. E., 2012, [Nature](#), **481**, 341

Virtanen P., et al., 2020, [Nature Methods](#), **17**, 261

Vogelsberger M., et al., 2014, [MNRAS](#), **444**, 1518

Wang J., Bose S., Frenk C. S., Gao L., Jenkins A., Springel V., White S. D. M., 2020, [Nature](#), **585**, 39

Witt H. J., Mao S., 1997, [MNRAS](#), **291**, 211

Zavala J., Frenk C. S., 2019, [Galaxies](#), **7**, 81

Çağan Şengül A., Tsang A., Diaz Rivero A., Dvorkin C., Zhu H.-M., Seljak U., 2020, [Phys. Rev. D](#), **102**, 063502

van der Walt S., Colbert S. C., Varoquaux G., 2011, [Computing in Science Engineering](#), **13**, 22